Yushu Xie (Orcid ID: 0000-0002-9956-0117)
Bruce W. Melville (Orcid ID: 0000-0001-8377-0403)
Asaad Y. Shamseldin (Orcid ID: 0000-0002-1701-7218)
Colin N. Whittaker (Orcid ID: 0000-0003-0283-8379)
Yifan Yang (Orcid ID: 0000-0002-8205-9617)

Direct measurement of the inertial drag and lift forces on entrained coarse particles at various protrusion heights

Yushu Xie [1,*]; Bruce W. Melville [1]; Asaad Y. Shamseldin [1]; Colin N. Whittaker [1]; Yifan Yang [1,2]

[1] Department of Civil & Environmental Engineering, The University of Auckland, Auckland 1142, New Zealand

[2] School of Engineering, The University of Waikato, Hamilton 3126, New Zealand

[*]Corresponding author: Yushu Xie (yxie399@aucklanduni.ac.nz)

Key Points:

- Inertial forces results reveal that the protrusion has less impact on the entrainment when the relative protrusion is more than 0.62-0.7.
- Inertial force coefficients remain constant when the relative protrusion is less than 0.62-0.7.
- Normalized inertial forces follow a linear relationship with Shields number under the present experiment condition.

Abstract

Laboratory experiments were performed to study the impact of the relative particle protrusion P/D (P is the protrusion height and D is the diameter of the target particle) on the mechanism of entrainment of sediment particles from a spherical rough bed. The target particle to be entrained was instrumented with electronic sensors, which can measure the tri-axis linear acceleration, and consequently the inertial hydrodynamic forces, during the entrainment process. The velocity field was obtained using the two-dimensional Particle Image Velocimetry (PTV) technique and the velocity data were synchronised with the force data relative to the entrainment time. Experimental results show that the magnitudes of inertial drag force and lift force have a decreasing trend as particle protrusion increases. The ratio of inertial lift force to drag force reveal that drag force slightly dominates the entrainment process at $P/D > 0.7$ while lift force slightly dominates at $P/D < 0.62$. Also, the inertial drag and lift coefficients were computed by the force data and velocity data. The inertial drag coefficient was found to be independent of P/D when $P/D < 0.62$ but declined with increasing P/D for $P/D > 0.62$. Similarly, the variation of inertial lift coefficient with P/D reversed at $P/D = 0.7$. This variation of force coefficients with P/D is consistent with the independence of inertial forces with respect to P/D when $P/D > 0.62$-0.7. In summary, the inertial forces demonstrate that the impact of protrusion on the particle entrainment becomes less important when $P/D > 0.62$-0.7.

Key words: Inertial drag force; inertial lift force; entrainment; relative protrusion;

1 Introduction

Through the erosion and deposition process, sediment transport contributes significantly to the natural evolution of river bed morphology (Recking et al., 2015) and also affects the aquatic habitat (Riebe et al., 2014). Sediment transport is a widely considered issue in water resources engineering and is a crucial consideration in areas such as the drainage of sediment deposition in a reservoir (Rahmani et al., 2018), erosion of the foundation of a hydraulic structure (Wang et al., 2018; Yang et al., 2019), and channel stability (Turowski et al., 2009). To address these issues, the critical condition for the initial movement of sediment particles is fundamentally important.

Generally, the critical condition of initial sediment movement can be determined using either deterministic (Zanke, 2003; Ali & Dey, 2016) or stochastic (Wu & Chou, 2003; Bose & Dey, 2013) approaches. Among the numerous studies on this topic, the classic work comprising the Shields parameter (Shields, 1936) has been widely used due to its simplicity of application and the apparent physical definition of the parameter. The critical Shields parameter θ_c is calculated by the following equation:

$$\theta_c = u_*^2/[(\rho_s/\rho\text{-}1)gD] \quad (1)$$

where u_* is the shear velocity, ρ_s is the sediment density, ρ is the fluid density, g is the gravitational acceleration, and D is the sediment diameter. θ_c is plotted against the particle Reynolds number Re_* ($Re_* = u_*D/\nu$, where ν is the fluid viscosity) in the original Shields diagram with the experimental data. The Shields diagram is widely used as a standard method to obtain the threshold condition of sediment motion, and considerable efforts have been made to explain the data scatter in the diagram (Buffington and Montgomery, 1997; Paphitis, 2001). However, the single Shields number is not suitable for predicting the wide range of threshold conditions for particle motion, even for an idealised particle. Many complex variables (bed irregularity, turbulence, etc.) need to be taken into account (Wiberg and Smith, 1987; Wilcock et al., 2003; Lamb et al., 2008; Dey & Ali, 2017). It is hard to consider a universal criterion of entrainment for all circumstances. In this study, the impact of particle protrusion on the initial particle movement is studied.

Bed irregularity may result in different protrusion heights of the sediment particles and affect the movability of equivalent particles. Fenton and Abbott (1977) pointed out that the original experiments used for the proposal of the Shields diagram were established on a relatively flat bed where no prominent protrusions can be observed. Therefore, they performed experiments in which the target particle was placed on a vertical rod and was extended into the water with various protrusion heights, thereby allowing investigation of the critical Shields number at different particle protrusion heights. Their experimental results indicate that the protrusion height has a significant impact on the critical Shields number. They also reported a critical value of 0.01 for a high protruding particle, which is considerably smaller than the commonly used Shields value, i.e. 0.03 – 0.06. Following the research of Fenton and Abbott (1977), Chin (1985) improved the experimental method and verified the importance of particle protrusion on the initial particle movement. Fenton and Abbott (1977) suggested that the Shields parameter has the minimum value of 0.01 at relative protrusion $P/D = 0.82$. The ratio $P/D = 0.82$ (P is the particle protrusion height and D is the diameter of the entrained particle) is the highest protrusion the target particle can reach when seated on the roughness particles with the same diameters (calculated from the local geometry relationship, assuming that the particles have spherical shape). Chin (1985) verified this value but suggested that a smaller value may be obtained at a higher protrusion height. Coleman et al. (2003) investigated the influence of particle protrusion on initial particle movement for crushed rock particles. In their experiments, square-shaped particles with various lengths and heights were used. They used similar experimental procedures to Fenton and Abbott (1977) and found that the critical Shields number of cuboid particles is smaller than that of spherical particles at the same protrusion, and also has a decreasing trend as the protrusion height increases.

Comparison of the results of Coleman et al. (2003), Fenton and Abbott (1977) and Chin (1985) reveals the vital role of particle protrusion in the initial particle movement for spherical particles and also for cuboid particles. In addition to experimental research on the protrusion effect, some analytical methods also involve the protrusion height effect. Dwivedi et al.(2012) proposed a new

Shields-type parameter to quantify the threshold flow condition, in which a modified factor is used to represent the protrusion height effect. In general, high protrusion not only contributes to the stronger movability of single grains but also affects the total bed sediment flux (Masteller and Finnegan, 2017; McKie et al., 2021). A highly protruding sediment grain provides a shelter region for the nearby sediment particles by preventing the shear region from approaching the bed surface (Raus et al., 2019). However, after removing the high protruding grain, the nearby stabilised sediment particles are more exposed and susceptible to erosion. Using flume experiments, Masteller and Finnegan (2017) highlighted a significant correlation between the fraction of highly protruding particles (determined from the variation of sediment elevation) and the total sediment transport rate. Overall, the influence of particle protrusion on sediment transport is significant from the grain scale to the macro fluvial reach scale.

As summarised, scientific works have been conducted to clarify the importance of particle protrusion in the initial sediment movement. However, most experimental studies have focused on investigating the flow characteristics rather than measuring the hydrodynamic forces acting on the particles with different protrusion heights. Analysis of the disequilibrium of the forces applied to a particle is the basis of determining the critical condition, especially for the establishment of theoretical models (Vollmer and Kleinhans, 2007; Ali and Dey, 2016). Therefore, some researchers have attempted to measure the hydrodynamic forces acting on a sediment particle under various circumstances (Fischer et al., 2002; Cameron et al., 2019; Bin Riaz et al., 2021) and tried to link them to the turbulent flow (Schmeeckle et al., 2007; Dwivedi et al., 2010a) or the averaged flow characteristics (Lamb et al., 2017). However, there remain limitations regarding the force measurement methods. Load cells or pressure sensors are commonly employed to investigate the hydrodynamic forces. The target particle is fixed to a mechanical sensor. Because the particle movement is restricted, the load cell can only record the force data until the particle is dislodged.

In recent years, advanced electronic techniques have brought a new possibility for sediment transport research. Some researchers placed accelerometers inside artificial or natural sediment particles (Kularatna et al., 2005; Abeywardana et al., 2009; Frank et al., 2014a) to investigate particle entrainment. Once the assembled particle moves, the embedded sensors can start recording the acceleration data. The acceleration data are transformed to the exerted forces by multiplying the particle mass. This new approach has been applied to impact force measurement (Spreitzer et al., 2019; Shafiei et al., 2016), monitoring river bed scour and sediment transport (Gendaszek et al., 2013; Olinde and P.L.Johnson, 2015; Stephenson and Abazović, 2016; Radchenko, 2017), and initial particle motion (Frank et al., 2014b; Maniatis et al., 2017; Maniatis et al., 2020). The concept of using instrumented accelerometers to measure the hydrodynamic forces exerted on the target particle has a distinct difference from the previously invasive methods. Since the accelerometers are instrumented inside the target particle, the flow in the vicinity of the target particle is not disturbed, and the actual entrainment condition is

provided. Without requiring the restriction of movement, the recorded acceleration can directly reflect the particle dynamics during the entrainment process. Compared with previous research, this method provides precious information for the particle entrainment mechanism and direct measurement of the applied force during the movement process.

The main objective of this study is to investigate the impact of particle protrusion on the entrainment process using instrumented sensors. The sensors can directly measure the inertial forces acting on the destabilised particle and, monitor the instantaneous dynamic features after entrainment. The present study not only helps to strengthen the understanding of entrainment mechanism but also provides a new insight on data acquisition and analysis.

2 Experimental apparatus

2.1 Flume and particle protrusion setup

Experiments were conducted in a 12 m long and 0.44 m wide recirculating tilting flume. A grid-shaped guide vane and straightener were installed to reduce the water surface undulation at the inlet of the flume. The flume has glass sidewalls that make the observation of the sediment particle movement clear and convenient (Figure 1a). The slope of the flume can be adjusted through the in-built jacking system with a maximum slope of 1%. The adjustment of the flume slope ensures a uniform flow condition during the experiments, with a range of approximately 0.04 – 0.08%. A pavement layer of plastic spheres was used to create a rough bed in a close hexagonal-packed pattern. The interstice formed by three adjacent packed particles provided the pocket for the target particle's placement (as shown in Figure 1b). The term "target particle" is used to refer to the spherical particle that is entrained in the experiments. The spherical roughness layer has a length of 4.5 m which ensures the full development of the flow structure. A 1.2 m long transition region composed of 2 – 3 cm natural coarse pebbles was installed upstream and downstream of the roughness layer. The deployment of the transition region aimed to reduce extra disturbance resulting from the abrupt change of the bed geometry. The test area was 4.7 m downstream of the entrance of the complete roughness layer. Four tape rulers (with a measurement accuracy of 0.5 mm) were attached to the sidewall of the flume with a space of 0.5 cm upstream of the target particle. The measured flow depths confirmed uniform flow conditions.

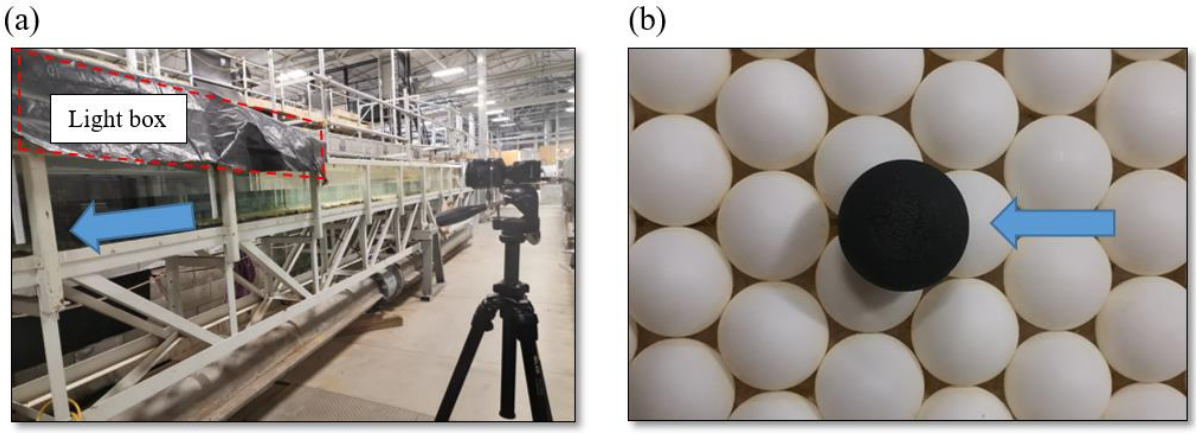

Figure 1. Flume setup, the blue arrow indicates the main flow direction. (a) Location of the light box and the camera; (b) target particle setting on the bed roughness particles.

The velocity field was measured using two-dimensional Particle Tracking Velocimetry (PTV). Tracer particles were fed into the recirculated flow and illuminated by the light-box. The light-box is a light source comprising an LED light array and fixing boards. Two boards are fixed together with screw systems, resulting in a small slit (5 mm) from which the lights are focused into a thin strip. The illuminated microparticles are neutrally buoyant and move in the flow direction. Their paths are captured by the camera located at the left side of the flume at a 1.2 m distance from the flume side wall. The position of the camera and the light-box are shown in Fig. 1a. Apart from the light-box, other indoor lights would be turned off during experiments. Also, the light-box was covered by black plastic cloth, which avoided extra ambient light from the outside environment. The camera operates at a frequency of 100 Hz, as is the sampling frequency of the acceleration measurement (described in the next section). The captured images are analysed for generating the flow field information by *Streams*, a software developed by Dr Nokes from the University of Canterbury, New Zealand. More information can be found in Nokes (2019).

As mentioned above, the spherical target particle was placed in the pocket formed by three adjacent spherical particles. From the known diameter sizes, the protrusion height P of the target particle above the top of surrounding roughness spheres can be computed. Two sizes of target particles with diameters of 30 mm and 40 mm, and two sizes of roughness spheres with diameters of 40 mm and 27 mm were used, resulting in four protrusion heights P = 21.3 mm (30 mm target particle over 40 mm roughness spheres), 25.4 mm (30 mm target particle over 27 mm roughness spheres), 32.6 mm (40 mm target particle over 40 mm roughness spheres), and 36.2 mm (40 mm target particle over 27 mm roughness spheres). Additionally, some specially designed three-dimensional models were employed to increase the target particle protrusion range. The schematic design for the three-dimensional model supporting the 30 mm target particle at P = 16 mm is shown in Figure 2. The top part of the model has a spherical shape, and the bottom part is a cylinder. With this design, the downstream face of the target particle is supported by two adjacent roughness spheres. The upstream face of the target particle is

supported by the top sphere connected to the cylinder. This design maintains the geometry consistency (comparing Figure 1b and Figure 2a) and reduces the gap between the target particle and bed roughness caused by the particle protrusion. By this method, three absolute particle protrusions (P = 16, 18, and 20 mm) were achieved for the target particle of 30 mm on the 40 mm bed spheres. Another two absolute particle protrusions (P = 25, 30 mm) were achieved for the target particle of 40 mm on the 40 mm bed spheres. Overall, nine absolute protrusions were used, resulting in nine relative particle protrusions P/D (D is the diameter of the target particle).

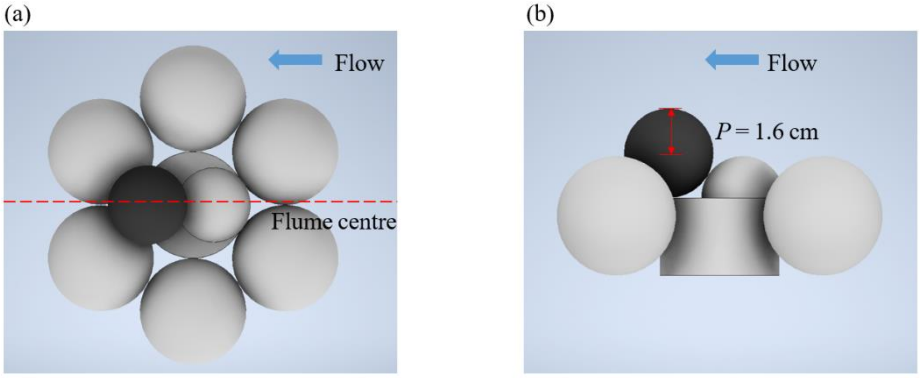

Figure 2. Particle protrusion setup design, take the example of P = 16 mm. (a) plan view; (b) side view; the blue arrow denotes the main flow direction.

During an entrainment experiment, the flow rate is slowly increased until initial particle movement is triggered. After each adjustment, the flow rate remained constant for 10 seconds to check whether the entrainment occurred. Preliminary experiments were conducted prior to the formal entrainment experiments. The preliminary experiments were used to decide the appropriate flow range for the particle entrainment at a specific particle protrusion. Then, the formal entrainment experiments were started at a close-to-threshold condition flow rate. The flow depth was measured from the theoretical bed elevation Z_0. There is no standard definition of the theoretical bed elevation for a rough bed, although it should be in the range of $0 - k_s$, where k_s is the roughness height which can be taken as the diameter of the roughness spheres when the bed is made of regular spherical elements (Dong et al., 1991). The value used varies amongst the data from different sources (Nezu and Nakagawa, 1993). In this study, the theoretical bed level where the velocity equals zero is defined as 0.2 d (d is the diameter of the spherical roughness elements). The value 0.2 d follows previous research (Cameron, 2006; Dwivedi, 2014), which used a similar experimental setup to the present study, and is in the range of $0.15 - 0.3\ k_s$, as suggested by Nezu and Nakagawa (1993). A flow depth of 203 mm was used for all experiment series, measured from the theoretical bed level. The coordinate system of measurement adopted the right-hand rule, with the positive X-axis along the mainstream direction and the positive Z-axis pointing to the flow surface. Since the target particle was always placed at the flume centre line, the origin of the coordinate system was at the flume centre line (Y = 0), 0.2 d below the roughness top

208 (Z = 0), and the target particle centre line (X = 0). The experimental setup and flow conditions are
209 summarised in Table 1.

210 **Table 1.** Summary of the case conditions

Case number	Q (l/s)	H (mm)	D (mm)	d (mm)	P (mm)	P/D (-)	U_{avg} (m/s)	Re $\times 10^3$ (-)	Fr (-)
Case 1	27.7	203	30	40	16	0.53	0.31	25.4	0.34
Case 2	24	203	30	40	18	0.6	0.268	21.9	0.30
Case 3	21.7	203	30	40	20	0.67	0.243	19.9	0.27
Case 4	18.9	203	30	40	21.3	0.71	0.212	17.4	0.24
Case 5	18.6	203	30	27	25.4	0.85	0.209	17.1	0.23
Case 6	30.8	203	40	40	25	0.62	0.344	28.2	0.38
Case 7	25.4	203	40	40	30	0.75	0.285	23.3	0.32
Case 8	20.8	203	40	40	32.6	0.82	0.232	19.0	0.26
Case 9	20.5	203	40	27	36.2	0.9	0.23	18.8	0.26

211 Note: Q denotes flow rate; H is flow depth from the 0.2 d below the roughness elements; D is the diameter of the
212 target particle; d is the diameter of the roughness spheres; P is the absolute protrusion height of the target particle
213 from the roughness top; P/D is defined as the relative protrusion height; U_{avg} is the cross-sectional velocity
214 calculated by the flow rate; Re is Reynolds number, and Fr is Froude number, calculated with the U_{avg}.

215 2.2 Measurement of the inertial hydrodynamic force on the entrained particle

216 The target particle was instrumented with an electronic board, including a tri-axis
217 accelerometer, tri-axis gyroscope, and tri-axis magnetometer. With the instrumented sensors, the linear
218 acceleration of the target particle is known during the dislodgement process. The plan and side view of
219 the electronic units are shown in Figure 3. The coordinate system of measurement is deployed at the
220 top left corner in Figure 3a and Figure 3b. The electronic board is a commercial product from the
221 Mbientlab Company (San Francisco, CA, USA), which can be used for multi-purpose motion tracking.
222 The electronic board is powered by a replaceable lithium coin battery installed on the backside of the
223 board (Figure 3b). The manufacturer provides software for remote controlling the manipulation and
224 data transmission, and the measured data were stored onboard temporarily and downloaded after the
225 experiment was finished. The storage space of the memory unit allows a consistent measure time of up
226 to four minutes with a 100 Hz sampling frequency.

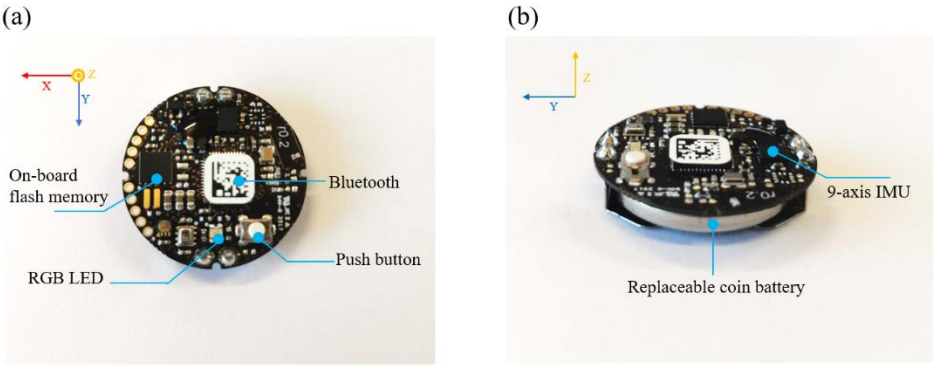

Figure 3. The embedded electronic board in the target particle: (a) plan view; (b) side view

The spherical enclosures were specially designed to house the electronic units and protect them from water damage. Two different sizes of spherical enclosure were designed, with an outside diameter of 30 mm and 40 mm, respectively. The 30 mm enclosure is shown in Figure 4a - 4b, and Figure 4c – 4d demonstrates the 40 mm enclosure. Both enclosures comprised two hollow hemispheres, which can be screwed together at the centre plane. The bottom hemisphere of the enclosure was designed to keep the electronic board stable and on the centre plane. The junction of the two hemispheres was filled with a thin layer of silicon glue to prevent water leakage. The materials of the two enclosures are carbon fibre for the 30 mm target particle and aluminium for the 40 mm target particle. The enclosure material requires good waterproofing capacity and data transmission performance. For the 30 mm target particle enclosure, three-dimensional printing technology was employed for the manufacturing. However, the carbon fibre material is too light for the 40 mm particle enclosure to maintain the density consistency. Therefore, aluminium was chosen to manufacture the 40 mm particle enclosure. Both particle enclosures have a smooth surface and are painted with a black colour to reduce light reflection. The complete particles had almost the same density of 1136.37 kg/m^3 and 1136.72 kg/m^3, respectively.

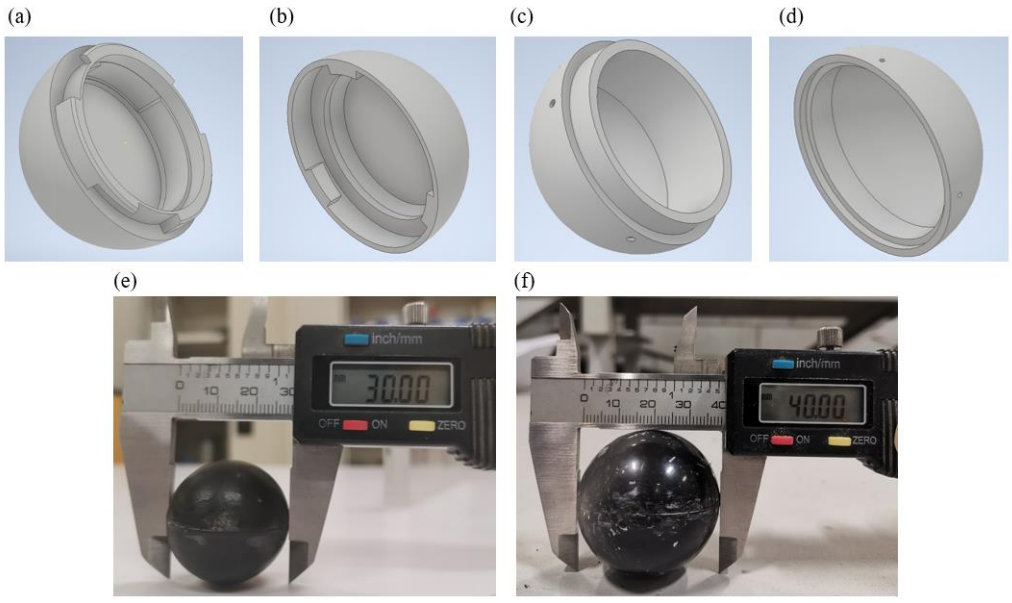

Figure 4. Enclosure and package of the target particle (TP): (a) the bottom part of the enclosure of TP-1; (b) the top part of the enclosure of TP-1; (c) the bottom part of the enclosure of TP-2; (d) the top part of the enclosure of the TP-2; (e) the assembled TP-1 and its dimension; (f) the assembled TP-2 and its dimension.

As mentioned previously, the velocity measurement frequency was set to 100 Hz to maintain synchronisation with the force measurement. Two sets of measurement data were synchronised at the particle entrainment time. The entrainment time was determined by inspecting the elevation change of the target particle among all the images. The entrainment time can also be determined from the time history of the acceleration data. The target particle is assumed to be entrained when its acceleration magnitude continuously surpasses the threshold noise level of the accelerometers (0.03 m/s^2). The threshold noise level is considered as the standard deviation of the acceleration when the accelerometer is kept stationary. Electronic sensors have signal noise even with the most accurate manufacturing techniques (Kok et al., 2017). In spite of the inevitable noise, accelerometers still have good performance and potential for capturing the particle dynamics during the movement process (Maniatis et al., 2017; Maniatis et al., 2020). After determining the exact entrainment time, the two sets of the measured data were synchronised. The tri-axis acceleration was then transformed to force data by multiplying by the target particle mass. The transformed force directly reflects the particle dynamics and is termed the inertial hydrodynamic force herein.

3 Inertial forces acting on the target particle

3.1 Tri-acceleration time histories for various particle protrusions

The tri-axis linear acceleration during a very short time (0.15 s) was investigated. The period of 0.15 s was chosen for two reasons. First, the linear acceleration measurement accuracy could be maintained for only a short time, and secondly, the acceleration during this time reflects directly the dynamic response of the particle at the instant of the entrainment event. Considering the main objective of this paper is focused on the particle response at the instant of entrainment, analysing the tri-axis linear acceleration during that short period is appropriate. Figure 5 shows the time series of tri-axis linear acceleration at different particle protrusions, from 0.1 seconds, before the particle entrainment, to 0.15 seconds after the particle entrainment. In Figure 5, a_x, a_y and a_z represent the linear accelerations for X, Y, and Z axis direction, respectively. The vertical dotted lines in these graphs represent the entrainment time $t = 0$. For each case, the entrainment time has been set to zero, which makes the comparison between different cases easier.

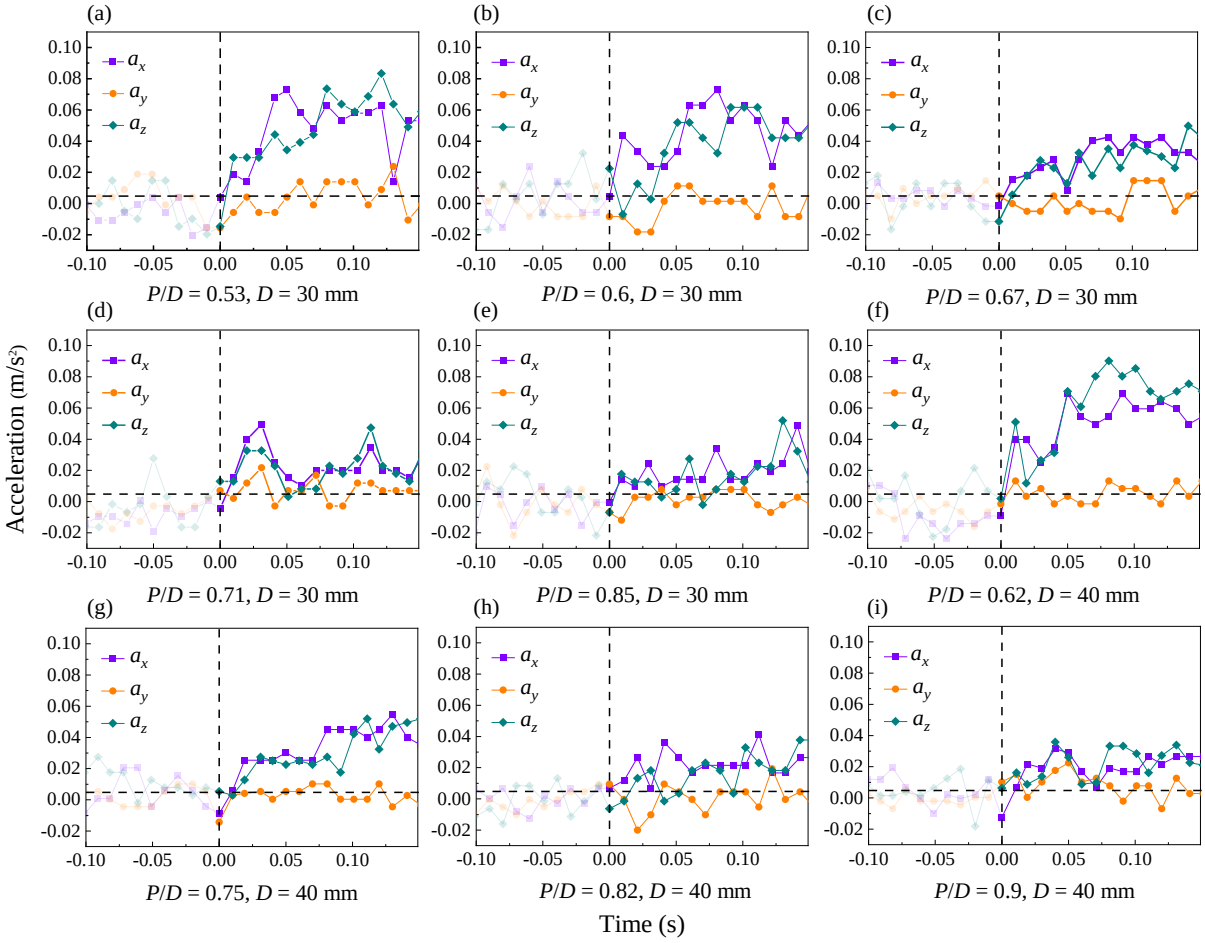

Figure 5. Tri-axis acceleration of the target particle before and after the entrainment for different P/D. (a) – (e) show the acceleration of 30 mm particle and, (f) – (i) show the acceleration of 40 mm particle.

Before $t = 0$, the target particle remains stationary. The fluctuations in the acceleration data before $t = 0$ are at the level of the signal noise (rather than being particle vibration), which was verified by inspecting the captured images. After $t = 0$, the variation of the acceleration magnitude exceeds the noise threshold indicating that the target particle starts moving. In Figure 5, it is apparent that the Y-axis acceleration magnitude is small for all protrusions relative to the X-axis and Z-axis accelerations. The Y-axis acceleration magnitude tended to remain at the level of background noise. The relatively small value of the Y-axis acceleration indicates that the target particle has no or minimal lateral movement during the entrainment process. Generally, the X-axis and Z-axis accelerations have comparable magnitudes at each time instant (except sometimes a_x exceeded a_z or vice versa) for all protrusion heights. The peak magnitude of the X-axis and Z-axis accelerations decrease from about 0.09 m/s^2 at P/D = 0.53, 0.62 to about 0.04 m/s^2 at P/D = 0.85, 0.9. The obvious drop of acceleration magnitude shows that particle protrusion has a significant influence on the hydrodynamic forces required for particle entrainment. It is also apparent that the peak magnitude of the acceleration is not solely dependent on the relative particle protrusion. For example, the peak acceleration at P/D = 0.6 (0.08 m/s^2) is smaller than that at P/D = 0.62 (0.09 m/s^2), and the peak acceleration at P/D = 0.71 (0.05

m/s^2) is smaller than that at P/D = 0.75 (0.06 m/s^2). The values of P/D = 0.6, 0.71 apply to the 30 mm target particle, while the values of P/D = 0.62, 0.75 apply to the 40 mm target particle. This difference implies that the particle size itself also affects the magnitude of the accelerations since a stronger force is required to "lift" a heavier object. However, this effect of particle size becomes less prominent for higher particle protrusions (P/D = 0.82, 0.85, and 0.9). The magnitude of tri-axis accelerations at these high protrusions are relatively similar.

3.2 Averaged inertial force during entrainment

In this section, the mean inertial force data, obtained by averaging the acceleration data over the time period of 0.15 s following particle entrainment, are discussed. The mean inertial force acting on the particle during the 0.15 s time period is determined as

$$\overline{F}_i = m\frac{\sum_0^t a_i \Delta t}{0.15} \tag{2}$$

where m is the mass of the target particle, with a unit of kg; Δt is the time interval of the measurement data = 0.01 s; a_i is the measured acceleration at each time instant; and t is the time period = 0.15 s. The computed mean forces in the X, Y and Z directions are plotted against the relative particle protrusions in Figure 6a – 6c. Also, the resultant inertial forces $\overline{F}_{iR}$, calculated on the basis of the tri-axis accelerations (shown in equation 2), are plotted in Figure 6d.

$$\overline{F}_{iR} = \sqrt{(\overline{F}_{ix})^2 + (\overline{F}_{iy})^2 + (\overline{F}_{iz})^2} \tag{3}$$

The data in the figures are grouped by the target particle size. Following the findings from Figure 5, the role of the Y-axis inertial force $\overline{F}_{iy}$ appears to be negligible compared with that of the other force components. For the current setup, the principal direction of movement of the entrained target particle is along with the X-axis and Z-axis directions. This result shows the entrainment path of the target particle is similar for different protrusion heights as expected because of the method of setting the protrusion heights, as discussed in Section 2. The geometrical set-up facilitates a focus on protrusion effects alone, eliminating other issues associated with the complexity of the overall entrainment process. The decreasing trends indicate that both $\overline{F}_{ix}$ and $\overline{F}_{iz}$ are inversely related to the relative particle protrusion height.

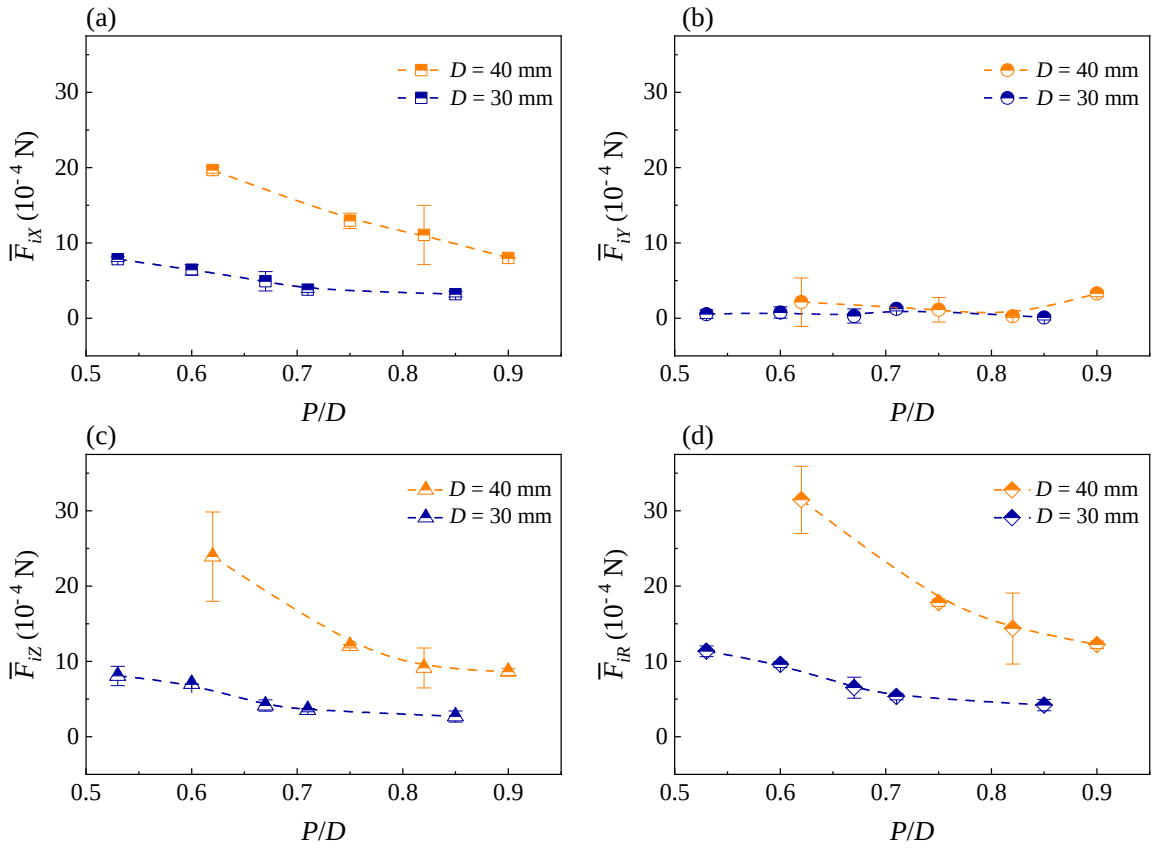

Figure 6. Averaged inertial (a) longitudinal, (b) lateral, (c) vertical, and (d) resultant forces for different *P*/*D*.

As pointed out in Figure 5, the particle size also impacts the magnitude of inertial forces. From Figure 6a, 6c, and 6d, the magnitudes of longitudinal, vertical and resultant inertial forces acting on the 40 mm target particle are always more significant than those on the 30 mm target particle at the same *P*/*D* value. The results for the 30 mm target particle show a 4.7×10^{-4} N reduction in $\overline{F}_{ix}$ and a 5.4×10^{-4} N reduction in $\overline{F}_{iz}$, from *P*/*D* = 0.53 to 0.85. The results for the 40 mm target particle show an 11.7×10^{-4} N reduction in $\overline{F}_{ix}$ and a 15.4×10^{-4} N reduction in $\overline{F}_{iz}$, from *P*/*D* = 0.62 to 0.9. These results show that the force decreases at a higher rate with increasing protrusion for the 40 mm particle, compared to that for the 30 mm particle. This is due to the protrusion increase having a more significant impact on the decrease of the acting force for coarser particles. The contribution of each axial force component to the resultant force is expressed as a percentage and is plotted against relative protrusion for each case in Figure 7. The percentage fluctuation of $\overline{F}_{ix}$ and $\overline{F}_{iy}$ varies slightly with particle protrusion for both target particle sizes and appears to do so independently of particle protrusion. The $\overline{F}_{ix}$ component fluctuates in a range of 40% - 50%, while $\overline{F}_{iy}$ varied between 0 – 20%. However, the $\overline{F}_{iz}$ component shows a slight decrease (from 50% - 40%) as the protrusion height increases.

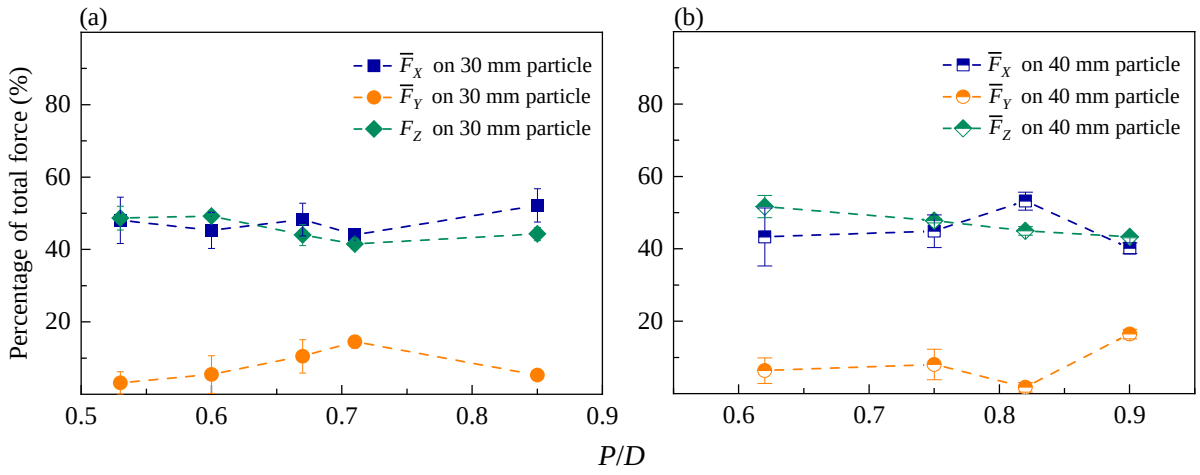

Figure 7. Percentage of tri-axial inertial forces for (a) 30 mm target particle and (b) 40 mm target particle at different P/D.

As discussed above, $\overline{F}_{iY}$ is relatively small compared to $\overline{F}_{iX}$ and $\overline{F}_{iZ}$, i.e., the force components exerted on the X-Z plane. This is because the present experimental setup limits the particle motion direction allowing focus on the protrusion effect on entrainment. In the present study, the inertial drag force $\overline{F}_{iD}$ can be obtained as follows:

$$\overline{F}_{iD} = \sqrt{\overline{F}_{iX}^2 + \overline{F}_{iY}^2} \tag{4}$$

The inertial lift force $\overline{F}_{iL}$ is represented by $\overline{F}_{iZ}$. The inertial drag and lift forces for both sizes of the target particles, normalised using the submerged weight of each target particle F_W, are plotted as a function of P/D in Fig. 8a and 8b, respectively. Normalisation using the submerged weight of each target particle means that the effect of the different particle sizes is included in the plot. Here, $\overline{F}_{iD}$ and $\overline{F}_{iL}$ data at P/D = 0.4 and 0.47 are added in Figure 8 and Figure 9. The experiments for the inertia forces measurement at P/D = 0.4 and 0.47 are not listed in Table. 1, because the synchronised velocity data were not measured. Therefore, the force data at P/D = 0.4 and 0.47 are only plotted in Figure 8 and Figure 9 as additional information, to better demonstrate the variation trend. The dashed lines (power functions), which demonstrate an inverse relationship between force and relative protrusion, are good fits to the data for the normalised inertial drag force (R^2 = 0.9) and lift force (R^2 = 0.8) within the range P/D = 0.53 to 0.9.

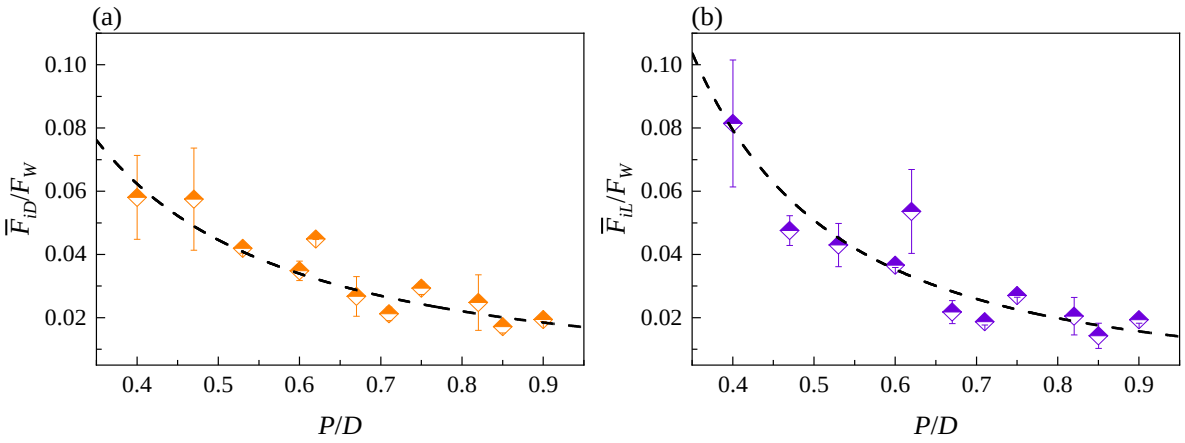

Figure 8. Normalised (a) drag force and (b) lift force for different particle protrusions

In general, $\overline{F}_{iL}/F_W$ and $\overline{F}_{iD}/F_W$ have similar magnitudes, but Figure 8a and 8b do not allow their individual effects on particle entrainment to be defined. For further analysis, the ratio of $\overline{F}_{iL}$ to $\overline{F}_{iD}$ is computed at each P/D value. The variation of $\overline{F}_{iL}/\overline{F}_{iD}$ with P/D is presented in Figure 9, in which the horizontal line represents the value of $\overline{F}_{iL}/\overline{F}_{iD} = 1$, i.e., the drag and lift components are equal. It is apparent that $\overline{F}_{iL}/\overline{F}_{iD} > 1$ occurs for $P/D < 0.62$ and $\overline{F}_{iL}/\overline{F}_{iD} < 1$ for $P/D > 0.67$. This result implies that a transition region exists between $P/D = 0.62$ and 0.67. The vertical line in the graph at $P/D = 0.65$ represents the transition region. The grey regions in Figure 9 encompass the two regions. They are defined by the ranges $P/D < 0.62$ and $\overline{F}_{iL}/\overline{F}_{iD}$ 0.8 – 1.5, and $P/D > 0.67$ and $\overline{F}_{iL}/\overline{F}_{iD}$ 0.7 – 1. It is clear that the inertial drag force commonly dominates in the entrainment process at high protrusion, while the inertial lift force becomes important at lower protrusions.

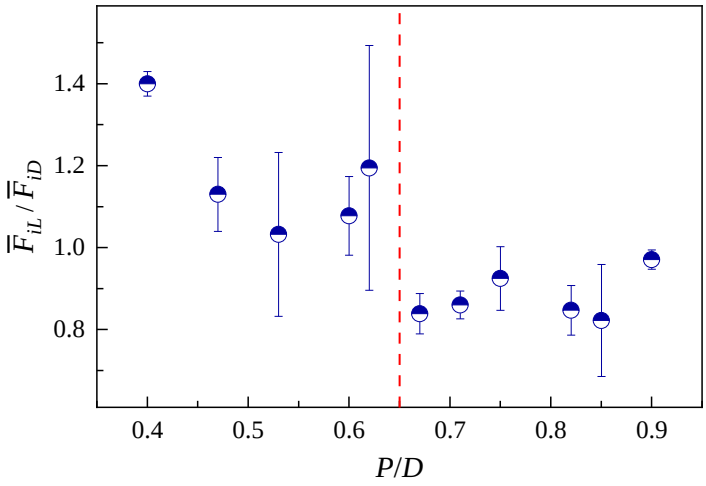

Figure 9. The ratio of inertial lift force to drag force

The averaged $\overline{F}_{iL}/\overline{F}_{iD}$ is about 0.9 for $0.67 < P/D < 0.9$, and about 1.1 for $0.53 < P/D < 0.62$. Both values indicate that the inertial drag and lift force have comparable impacts on the particle entrainment. The mode of movement of the target particle is also important and accounts for some of the difference in the force ratio values at entrainment. There are three modes of movement of sediment

particles: sliding, rolling, and saltation (Ancey et al., 2002; Ancey et al., 2003). A saltating particle begins moving with a vertical jump from the setting pocket, and the lift force may be dominant at the instant of entrainment. Compared with a saltating particle, a sliding/rolling particle has less strong vertical motion. A rolling particle rotates initially such that both drag and lift forces are important during entrainment. In this study, entrainment occurred due to rolling motion, which partly explains the similar magnitude of the measured inertial drag and lift forces. In the following section, the synchronised velocity data are presented and their link with inertial force is discussed.

4 Velocity and inertial forces

4.1 Double-averaged velocities at 0.15D above the target particle

A protruding target particle leads to heterogenous spatial distribution of velocity in the near bed region (Raus et al., 2019). Therefore, the double-averaged (both in time and space) velocity is considered appropriate to analyse its link with the mean inertial forces. The double-averaged concept is used by many researchers for the study of flow over a rough bed (Nikora et al., 2001; Dwivedi, 2014; Raus et al., 2019). It consists of average computation in the time domain, and spatial averaging along the horizontal plane parallel to the bed surface. In the double-averaged methodology, the time-averaged velocity can be decomposed into double-averaged and spatial averaged components, as follows:

$$\bar{U} = \left\langle \bar{U} \right\rangle + \tilde{U} \tag{5}$$

where the overbar and bracket denote the time average and spatial average, respectively, and the wave overline represents the spatial fluctuation. The average time period is 10 seconds prior to the particle entrainment. The spatially averaged window in this study is from 2*d* upstream to 2*d* downstream of the target particle centre (*d* is the diameter of the target particle). This averaging window is a compromise between ensuring enough length to include the velocity variation, while limiting the length of the window. Additionally, the double-averaged velocity is extracted from the measurement field at 0.15*D* above the target particle centroid. The vertical location of the specific velocity analysis is at $Z_m = 0.2d + P + 0.15D$ from the theoretical bed level. This location was chosen because Dwivedi et al. (2010b) found a maximum correlation between the instantaneous velocity and drag force at this height, and they used a similar experimental setup to the present study. In summary, the double-averaged longitudinal velocity $<\bar{U}_{0.15D}>$ and vertical velocity $<\bar{V}_{0.15D}>$ at Z_m are extracted from velocity field. The double averaged longitudinal and vertical velocity are plotted against the *P*/*D* in Figure 10a and 10b, respectively.

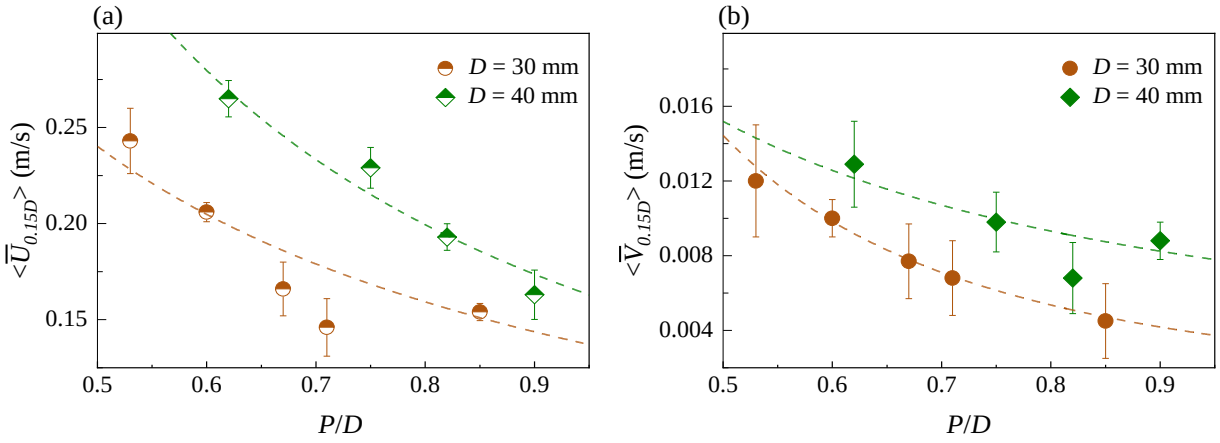

Figure 10. Double-averaged velocity at the height of 0.15 *D* above the target particle. (a) Longitudinal velocity; (b) vertical velocity.

Both $<\overline{U}_{0.15D}>$ and $<\overline{V}_{0.15D}>$ are inversely related to *P*/*D*, which is similar to the relationship between the inertial forces and *P*/*D*. The $<\overline{U}_{0.15D}>$ value for the target particle with 30 mm diameter is 0.243 m/s at *P*/*D* = 0.53, and drops to 0.154 m/s at *P*/*D* = 0.85. Interestingly, the lowest value $<\overline{U}_{0.15D}>$ = 0.146 m/s was found at *P*/*D* = 0.71. This suggests that the effect of particle protrusion becomes minimal when *P*/*D* > 0.71. The flow strength required for particle entrainment varies slightly between *P*/*D* = 0.71 and *P*/*D* = 0.85. Conversely, the value of $<\overline{U}_{0.15D}>$ decreased continually from 0.265 m/s to 0.153 m/s for the 40 mm target particle, with an obvious drop from *P*/*D* = 0.82 to 0.9. The value of $<\overline{V}_{0.15D}>$ decreased from 0.012 to 0.0045 m/s for the 30 mm target particle, and from 0.013 to 0.009 m/s for the 40 mm target particle.

4.2 Relationship between inertial forces and velocity

In this section, we further discuss the relationship between the inertial hydrodynamic forces and the velocities at different particle protrusion heights. The results could provide more information for developing a theoretical model to predict the threshold condition of particle entrainment. The inertial drag force F_{iD} and lift force F_{iL} exerted on the sediment particle are generally expressed in the following forms:

$$\overline{F}_{iD} = 0.5\rho C_{iD} \left\langle \overline{U}_{0.15D} \right\rangle^2 A \tag{6a}$$

$$\overline{F}_{iL} = 0.5\rho C_{iL} \left\langle \overline{U}_{0.15D} \right\rangle^2 A \tag{6b}$$

in which C_{iD} is the inertial drag coefficient, C_{iL} is the inertial lift coefficient, and *A* is the cross-sectional area of the target particle projected on the transverse plane of the flow above the bed roughness (related to the particle protrusion *P*). In order to simplify the calculation process, the cross-sectional area above the top of the surrounding bed roughness is used for the coefficient computation, following the research of Cameron (2006). The schematic graph of exposed area *A* at the absolute particle protrusion *P* is

shown in Figure 11, together with the computed results of A versus P/D. Equation 7a and 7b show the calculation of the exposed area, the results are summarised in Table 2.

$$\omega = 2\cos^{-1}\left(\frac{P - D/2}{D/2}\right) \tag{7a}$$

$$A = \left(1 - \frac{\omega}{2\pi}\right)\frac{\pi D^2}{4} + \frac{D}{4}\left(P - D/2\right) \tag{7b}$$

where ω is the radian of the obstructed area of the target particle (shown in Figure 11), and π is the mathematic constant.

Table 2. Summarised exposed area and the inertial drag and lift coefficients

	Case 1	Case 2	Case 3	Case 4	Case 5	Case 6	Case 7	Case 8	Case 9
A ($\times 10^{-4}$ m^2)	1.99	2.43	2.86	3.11	3.75	4.62	5.92	6.46	6.92
C_{iD} (-)	0.134	0.127	0.128	0.121	0.072	0.124	0.084	0.092	0.107
C_{iL} (-)	0.138	0.136	0.106	0.108	0.061	0.148	0.077	0.076	0.106

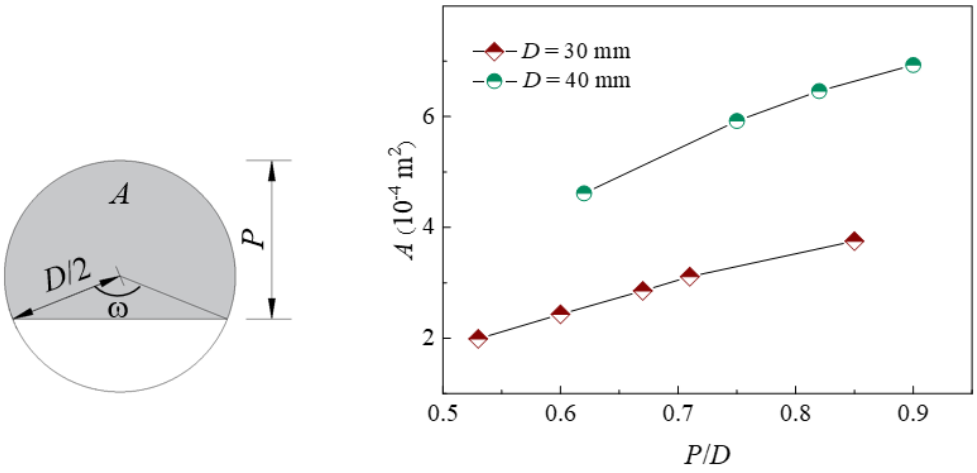

Figure 11. Schematic graph of the exposed area calculation and the computed results of A versus P/D

From Figure 11, it is seen that the exposed area of the target particle gradually increases with increasing P/D. The measured forces and the calculated values of $0.5\rho<\bar{U}_{0.15D}>^2 A$ are plotted in Figure 12a and Figure 12b. Also, the value of $0.5\rho<\bar{V}_{0.15D}>^2 A$ is calculated and plotted against the measured forces in Figure 12c and 12d, to demonstrate their correlation. From Figure 12a, it is apparent that both the inertial drag and lift forces are positively related to $<\bar{U}_{0.15D}>$. Also, the inertial drag and lift forces are positively related to $<\bar{V}_{0.15D}>$ (Figure 12b).

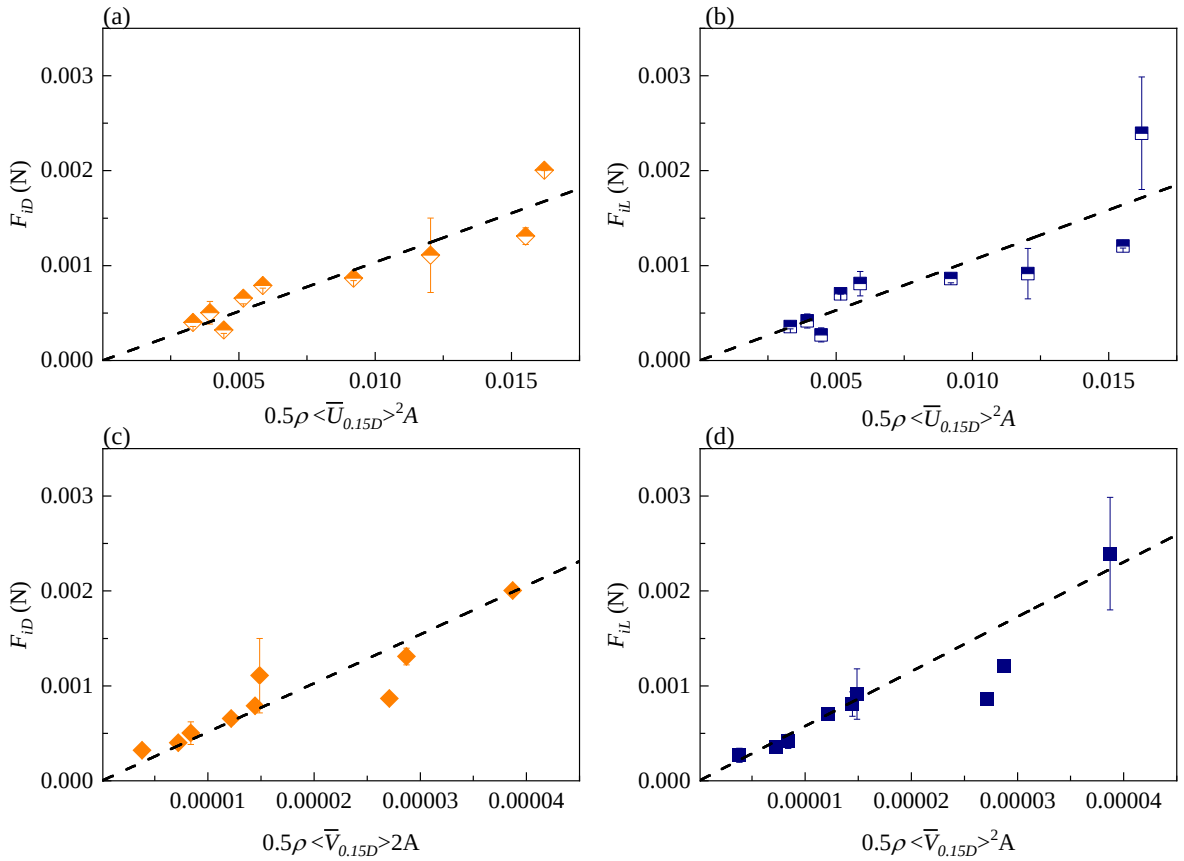

Figure 12. The relationship between the (a) $\overline{F}_{iD}$ and $0.5\rho<\overline{U}_{0.15D}>^2A$; (b) $\overline{F}_{iD}$ and $0.5\rho<\overline{U}_{0.15D}>^2A$; (c) $\overline{F}_{iD}$ and $0.5\rho<\overline{V}_{0.15D}>^2A$; (d)) $\overline{F}_{iD}$ and $0.5\rho<\overline{V}_{0.15D}>^2A$ .The error bars indicate the standard deviation of the repeated experiments.

In Figure 12, the dotted lines are plotted using regression analysis and indicate the linear relationship between the forces and $0.5\rho<\overline{U}_{0.15D}>^2A$ (or $0.5\rho<\overline{V}_{0.15D}>^2A$) values. The scatter in the data, especially at higher inertial force values, is due to a number of factors, including the simplified method adopted to define the exposed areas, the variation of the inertial drag and lift coefficients, the calculation of the velocity at a specific location, and the velocity fluctuations. These simplifications facilitate the variation of the inertial drag and lift coefficients with the relative particle protrusion P/D being the focus of the analysis. Using Equation 4a and 4b, the inertial drag coefficient C_{iD} and lift coefficient C_{iD} are calculated and plotted in Figure 13a and 13b as functions of P/D. The calculated results are summarised in Table 2.

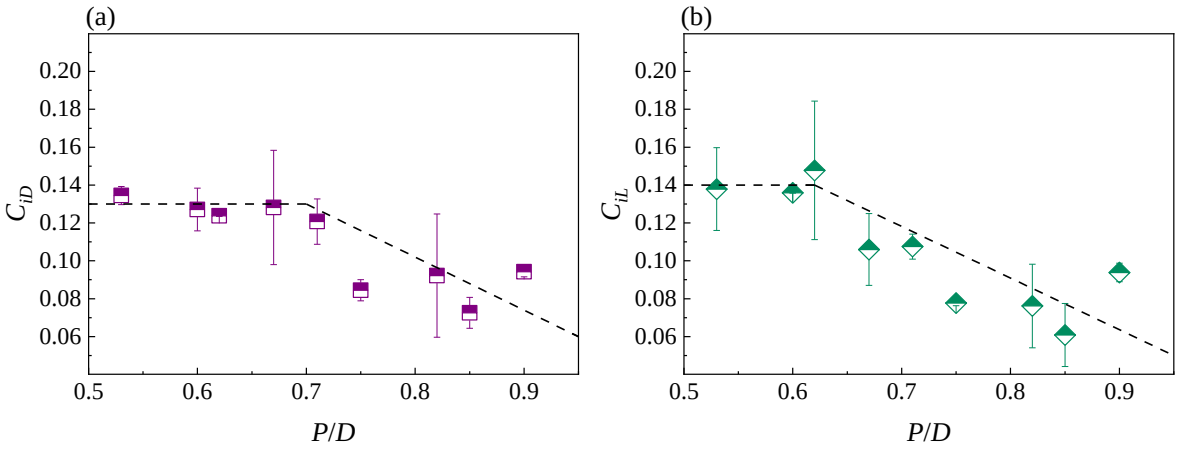

458

459 **Figure 13.** Inertial (a) drag coefficients and (b) lift coefficients at different *P*/*D*.

460 The inertial drag coefficient C_{iD} ranged from 0.08 to 0.13, and the lift coefficient C_{iL} ranged
461 from 0.06 to 0.14, indicating that is they have similar values over the range of *P*/*D* values investigated.
462 The inertial lift coefficient has a slightly higher value than the inertial drag coefficient for lower
463 protrusion cases (see Table 2: Case 1, 2, and 6), but a smaller value for the higher protrusion cases (see
464 Table 2: Case 3, 4, 5, 7, 8 and 9). Both the drag coefficient and the lift coefficient are relatively constant
465 at lower *P*/*D* (0.5-0.7) and decrease for $P/D \geq 0.7$. The particle protrusion affects the values of both the
466 inertial drag and lift coefficients for $P/D \geq 0.7$. In this range, the exposed frontal area of the target
467 particle increased (Figure 11b) but the inertial forces and $<\overline{U}_{0.15D}>$ values remained approximately
468 constant (Figure 8 and Figure 10a). According to Equation 4a and 4b, the force coefficients are
469 determined by *A*, $<\overline{U}_{0.15D}>$, $\overline{F}_{iD}$, and $\overline{F}_{iL}$. When the values of $<\overline{U}_{0.15D}>$, $\overline{F}_{iD}$, and $\overline{F}_{iL}$ remained
470 constant, the increased value of *A* results in a decrease of the force coefficients. In other words, the
471 turning points of the inertial coefficients with *P*/*D* are correlated to those of the inertial forces with *P*/*D*.
472 Here we noticed that the threshold *P*/*D* is 0.7 for drag coefficient variation (Figure 13a) and 0.62 for
473 lift coefficient (Figure 13b). As discussed above, this difference indicates that the inertial drag force
474 becomes stable when $P/D > 0.7$ and, inertial lift force approaches to be constant when $P/D > 0.62$
475 (Figure 8).

476 **5 Critical Shields number**

477 In this section, the critical Shields numbers θ_c (defined in Equation 1) for different particle
478 protrusions are investigated to clarify the particle protrusion effect. θ_c is calculated on the basis of shear
479 velocity U_*. There are many methods for the shear velocity calculation (Biron et al., 2004). In the
480 research of Nikora et al. (2001), the ratio of H/k_s (*H* is the flow depth and k_s is the roughness height) is
481 used to define the flow type. In the present study, H/k_s is 5.1 for flow over the 40 mm roughness bed,
482 which is classified as Type Ⅱ flow. For Type Ⅱ flow, the Reynolds shear stress profile seems to be the
483 most appropriate method to calculate the shear velocity since the formation of the logarithmic region is

uncertain in this flow type. Specifically, the double-averaged Reynolds shear stress profile is extrapolated to the bed for obtaining the shear stress and computing the shear velocity. The calculated U_* and θ_c value are listed in Table 3 and plotted in Figure 14a.

Table 3. Shear velocity and critical Shields number

	Case 1	Case 2	Case 3	Case 4	Case 5	Case 6	Case 7	Case 8	Case 9
U_* (cm/s)	3.26	2.49	1.99	1.50	1.32	3.00	2.43	2.15	1.54
θ_c (-)	0.028	0.016	0.010	0.006	0.004	0.018	0.012	0.009	0.005

As expected, the effect of relative particle protrusion on the critical Shields number is significant. When P/D increased from 0.53 to 0.9, θ_c decreased from 0.03 to 0.005. It is also noticed that θ_c has a slower decrease rate starting from P/D = 0.65 and gradually becomes approximately constant for $P/D \geq 0.85$. The decreasing trend of θ_c with P/D is consistent with the variation of inertial forces (Figure 8) and mean velocities (Figure 10) with P/D. For comparison, the present experimental results are plotted together with previous research results (Fenton and Abbott, 1977; Chin, 1985; Cameron, 2006; Dwivedi et al., 2012) in Figure 14b. The present experimental data agree well with the previous results. Coleman et al. (2003) propose a best-fit expression to describe the relationship between θ_c and the protrusion of spherical particles, as follows:

$$(\theta_c - 0.002) = 0.016(P/D)^{-1} \tag{8}$$

For this equation, the constant 0.002 is adopted as the lower bound of the critical Shields number. As shown in Figure 14a, the lower bound of the Shields parameter, based on the present data, is about 0.005, larger than that suggested by Coleman et al. (2003). Using the present data, combined with the results from the relevant literature, an alternative expression is derived (Equation 9). The correlation factor for this relationship is about 0.88, indicating a good match with the measured data.

$$(\theta_c - 0.005) = 0.1392e^{-3.267(P/D)} \tag{9}$$

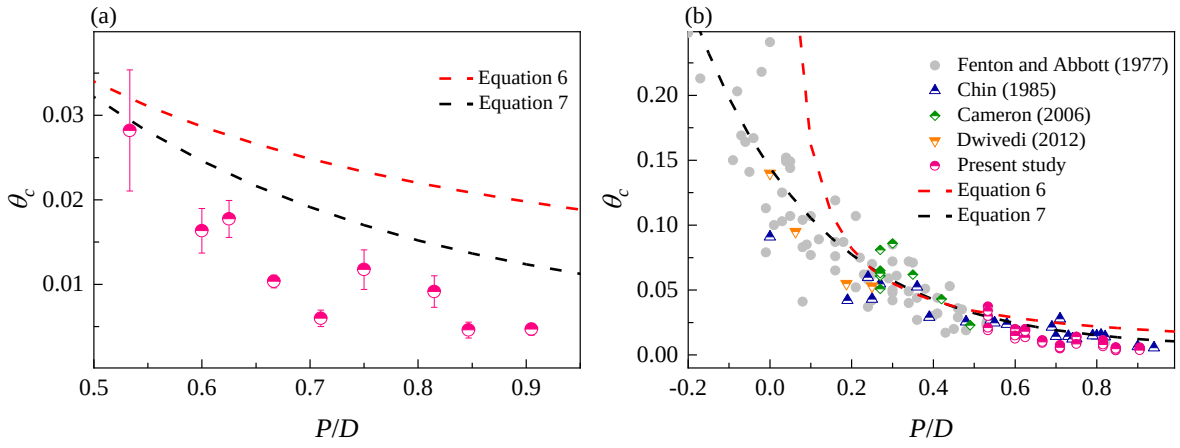

Figure 14. Shields number at different P/D. (a) present results; (b) comparison with previous research.

Fenton and Abbott (1977) suggested that the critical Shields number has a minimum value of 0.01 at P/D = 0.82. The value P/D = 0.82 represents the protrusion when the spherical target particle stays at the interstice formed by three densely packed spherical roughness particles with the same diameter. In the present study, θ_c has a value of 0.009 for P/D = 0.82 (representing the 40 mm target particle on the 40 mm bed), matching the results from Fenton and Abbott (1977). However, as pointed out previously, the lowest value of θ_c in the present study is 0.005 for P/D = 0.85 and 0.9, which is clearly smaller than 0.01. The difference is due to the different procedures used for the entrainment experiments. In the experiments of Fenton and Abbott (1977), the target particle was attached to the top of a rod that was installed on the flume bed. Under a predetermined flow condition, the rod was extended into the flow at a slow speed until the initial movement of the target particle occurred. After the entrainment experiment, the elevation of the rod was recorded and used to calculate the particle protrusion. Fenton and Abbott (1977) suggested that this procedure did not ensure a reasonable period of flow acting on the target particle and tended to overestimate the θ_c. This limitation was also mentioned by Coleman et al. (2003), who conducted experiments to study the entrainment condition of a protruded prismatic square. The lower values of θ_c may also be related to the lower particle density. In general, the effect of particle protrusion on the critical entrainment condition is apparent in this study and consistent with previous results.

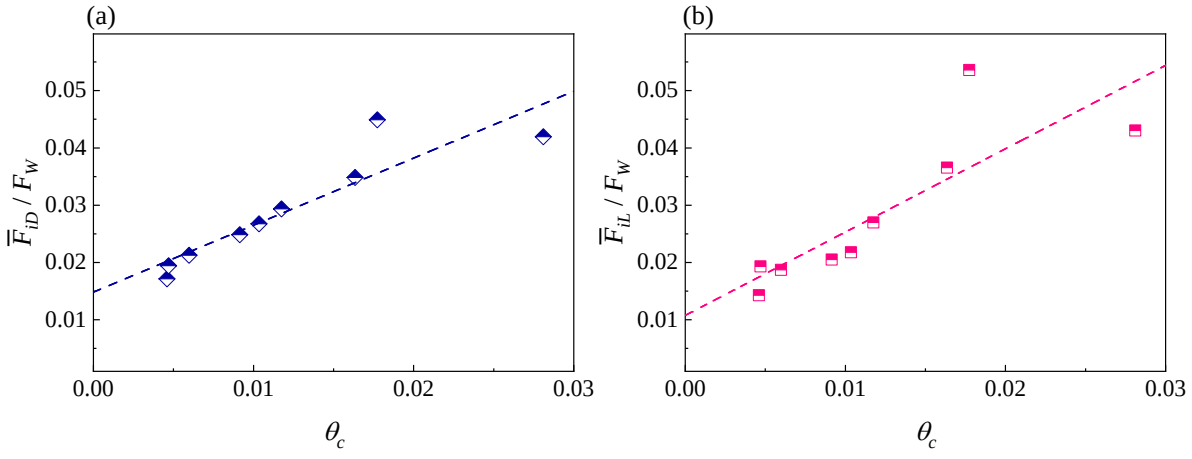

Figure 15. The relationship between normalised inertial (a) lift and (b) drag force and Shields number

The normalised inertial drag force ($\overline{F}_{iD}/F_W$) and lift force ($\overline{F}_{iL}/F_W$) are plotted against the critical Shields number in Figure 15 to examine their interdependence. From Figure 15, it is clear that both the inertial drag and lift force are positively related to the critical Shields number. Straight lines (dotted in the figure) are fitted to the data. The fitted lines show good agreement with the measured data (R^2 = 0.83 for Figure 15a, R^2 = 0.71 for Figure 15b). From the best-fit lines, $\overline{F}_{iD}/F_W$ is 0.015 for θ_c = 0 and 0.05 for θ_c = 0.03, while $\overline{F}_{iL}/F_W$ is 0.01 for θ_c = 0 and 0.055 for θ_c = 0.03. The values of $\overline{F}_{iD}/F_W$ are slightly higher than those for $\overline{F}_{iL}/F_W$ at lower θ_c (relative to higher P/D), and vice-versa at higher θ_c (relative to lower P/D).

6 Summary and Conclusions

Laboratory experiments to study the particle protrusion impact on the entrainment mechanism are reported. A tri-axial accelerometer was used to measure the inertial forces acting on the target particle during the entrainment process. The direct measurement of the inertial drag and lift forces at different particle protrusion heights provides novel insight into the particle entrainment mechanism.

The accelerations are transferred to inertial forces and averaged over the time period of 0.15 s after the particle entrainment. The mean Y-axial inertial force $\overline{F}_{iy}$ shows similar magnitude for different P/D. Both mean X-axial inertial force $\overline{F}_{ix}$ and Z-axial inertial force $\overline{F}_{iz}$ are inversely related to P/D. The $\overline{F}_{ix}$ and $\overline{F}_{iy}$ forces are combined to represent the inertial drag force $\overline{F}_{iD}$, while $\overline{F}_{iz}$ is regarded as the inertial lift force $\overline{F}_{iL}$. Both $\overline{F}_{iD}$ and $\overline{F}_{iL}$ decrease as the protrusion height increases. The normalised $\overline{F}_{iD}$ is 0.045 at P/D = 0.65, then decreases to 0.02 at P/D = 0.9. The normalised lift force has an equivalent variation range with that of the normalised drag force. The data are also interpreted in terms of $\overline{F}_{iL}/\overline{F}_{iD}$ which indicates that both $\overline{F}_{iD}$ and $\overline{F}_{iL}$ play essential roles in particle entrainment for the protrusion range covered by the present data, since the value of $\overline{F}_{iL}/\overline{F}_{iD}$ approaches 1. Nevertheless, the inertial lift force plays a more significant role in the entrainment process for $P/D < 0.65$ ($\overline{F}_{iL}/\overline{F}_{iD} > 1$). Conversely, the effect of drag force becomes predominant for $P/D > 0.65$ ($\overline{F}_{iL}/\overline{F}_{iD} < 1$). This result may generally be representative of entrainment by particle movement in the rolling mode, which involves both drag and lift forces. However, more detailed investigation of the effect of the entrainment modes on the inertial hydrodynamic forces is needed.

The double-averaged velocity at $0.15D$ above the bed level, in the stream-wise direction $<\overline{U}_{0.15D}>$ and vertical direction $<\overline{V}_{0.15D}>$, are found to be inversely related to the protrusion height $\overline{F}_{iD}$ and $\overline{F}_{iL}$ are strongly correlated with both $<\overline{U}_{0.15D}>$ and $<\overline{V}_{0.15D}>$. The inertial drag coefficient C_{iD} and lift coefficient C_{iL} are computed using $<\overline{U}_{0.15D}>$. The values of C_{iL} fluctuate around 0.14 for $P/D \leq 0.65$, reducing for higher values of P/D. Values of C_{iD} are relatively constant at about 0.127 for $P/D \leq 0.7$, decreasing for higher relative protrusion. The variation of C_{iD} and C_{iL} with P/D shows that the particle entrainment dynamics has two regimes depending on the relative protrusion, with a transition between regimes at P/D in the range 0.65–0.7.

Critical Shields number θ_c is computed and compared with previous research results, confirming the significance of particle protrusion in the entrainment process. The present results show good agreement with previous researches and extend the data for the medium to high protrusion range. Equation 9 is used to describe the variation between critical Shields number and protrusion height. Also, the relationship between the normalised inertial forces and θ_c is investigated. Generally, both $\overline{F}_{iD}/F_W$ and $\overline{F}_{iL}/F_W$ are linearly correlated with θ_c for $P/D < 0.65$, with lower confidence in this relationship for higher protrusions.

Overall, the protrusion height profoundly impacts the acting inertial forces during the entrainment process, including the magnitude, allocation of force components, and correlation to the local velocity and critical flow conditions.

Acknowledgement

This research is financially funded by the CSC (Chinese Scholarship Council) and the University of Auckland, New Zealand. The laboratory technicians at the University of Auckland helped with the design of the enclosure encompassing the electronic sensors and the setup of the experimental flume and related apparatus.

Data Availability Atatement

The link to download the experimental data is as follows: https://drive.google.com/drive/folders/1o50XAo6oypsYwV0iZkkSAlKx3rG8xQwG?usp=sharing

Annotation

P: Particle protrusion over the top of the surrounding roughness particle, mm;

D: Diameter of the target particle, mm;

$\overline{F}_{iL}$: Mean inertial lift force, N;

$\overline{F}_{iD}$: Mean inertial drag force, N;

F_W: Submerged weight, N;

θ_c: Critical Shields number;

U_*: Shear velocity, cm/s;

ρ_s: Sediment density, kg/m^3;

ρ : Fluid density, kg/m^3;

g: gravitational acceleration, m/s^2;

v: fluid viscosity, m^2/s;

Z_0: theoretical bed level, mm;

k_s: roughness height, mm;

Q: flow rate, l/s;

d: diameter of the bed roughness spheres, mm;

H: flow depth, mm;

U_{avg}: cross section averaged flow velocity, m/s;

Re: flow Reynolds number,-;

Fr: flow Froude number,-;

t: time, s;

m: mass of the target particle, kg;

Δt: time interval, s;

a_x, a_y, a_z: acceleration for X, Y, and Z direction, respectively, m^2/s;

602 $\overline{F}_{ix}$, $\overline{F}_{iy}$, $\overline{F}_{iz}$: mean inertia force for X, Y, and Z direction, respectively, N;

603 $\overline{F}_{iR}$: mean resulatant inertial force, N;

604 $<\overline{U}>$: double-averaged velocity, m/s;

605 $\overline{U}$: mean velocity, m/s;

606 $\widetilde{U}$: spatial fluctuation of mean velocity, m/s;

607 Z_m: elevation of velocity measurement location, mm;

608 $<\overline{U}_{0.15D}>$: double-averaged stream-wise velocity at 0.15 *D* above the target particle, m/s;

609 $<\overline{V}_{0.15D}>$: double-averaged vertical velocity at 0.15 *D* above the target particle, m/s;

610 *A*: cross-sectional area, m^2;

611 ω: radian of the obstructed area of the target particle, rad;

612 C_{iD}: inertial drag force;

613 C_{iL}: inertial lift force;

614 λ: the ratio of the prototype to the model scale;

615 Re_*: particle Reynolds number;

616 **References**

617 Abeywardana, D. K., Hu, A. P., & Kularatn, N. (2009). Design enhancements of the smart sediment
618 particle for riverbed transport monitoring. *2009 4th IEEE Conference on Industrial Electronics*
619 *and Applications, ICIEA 2009*, 336–341. https://doi.org/10.1109/ICIEA.2009.5138224

620 Ali, S. Z., & Dey, S. (2016). Hydrodynamics of sediment threshold. *Physics of Fluids*, *28*(7), 075103.
621 https://doi.org/10.1063/1.4955103

622 Ancey, C., Bigillon, F., Frey, P., & Ducret, R. (2003). Rolling motion of a bead in a rapid water stream.
623 *Physical Review E - Statistical Physics, Plasmas, Fluids, and Related Interdisciplinary Topics*,
624 *67*(1), 11. https://doi.org/10.1103/PhysRevE.67.011303

625 Ancey, C., Bigillon, F., Frey, P., Lanier, J., & Ducret, R. (2002). Saltating motion of a bead in a rapid
626 water stream. *Physical Review E - Statistical Physics, Plasmas, Fluids, and Related*
627 *Interdisciplinary Topics*, *66*(3), 1–16. https://doi.org/10.1103/PhysRevE.66.036306

628 Bin Riaz, M. Z., Yang, S., Sivakumar, M., Enever, K., Miguntanna, N. S., & Khalil, U. (2021). Direct
629 measurements of hydrodynamic forces induced by tidal bores. *Water Resources Research*, 1–17.
630 https://doi.org/10.1029/2020wr028970

631 Biron, P. M., Robson, C., Lapointe, M. F., & Gaskin, S. J. (2004). Comparing different methods of bed
632 shear stress estimates in simple and complex flow fields. *Earth Surface Processes and Landforms*,
633 *29*(11), 1403–1415. https://doi.org/10.1002/esp.1111

634 Bose, S. K., & Dey, S. (2013). Sediment entrainment probability and threshold of sediment suspension:
635 Exponential-based approach. *Journal of Hydraulic Engineering*, *139*(10), 1099–1106.

https://doi.org/10.1061/(ASCE)HY.1943-7900.0000763

Buffington, J. M., & Montgomery, D. R. (1997). A systematic analysis of eight decades of incipient motion studies, with special reference to gravel-bedded rivers. *Water Resources Research*, *33*(8), 1993–2029. https://doi.org/10.1029/96WR03190

Cameron, S. M., Nikora, V. I., & Marusic, I. (2019). Drag forces on a bed particle in open-channel flow: Effects of pressure spatial fluctuations and very-large-scale motions. *Journal of Fluid Mechanics*, *863*, 494–512. https://doi.org/10.1017/jfm.2018.1003

Cameron, Stuart M. (2006). *Near-boundary flow structure and particle entrainment*. Ph.D. thesis, the University of Auckland, New Zealand.

Chin, C. O. (1985). *Stream bed armouring*. Ph.D. thesis, the University of Auckland, New Zealand.

Coleman, S. E., Melville, B. W., & Gore, L. (2003). Fluvial entrainment of protruding fractured rock. *Journal of Hydraulic Engineering*, *129*(11), 872–884. https://doi.org/10.1061/(ASCE)0733-9429(2003)129:11(872)

Dey, S., & Ali, S. Z. (2017). Mechanics of sediment transport: Particle scale of entrainment to continuum scale of bedload flux. *Journal of Engineering Mechanics*, *143*(11). https://doi.org/10.1061/(ASCE)EM.1943-7889.0001343

Dong, Z., Wang, J., Chen, C., & Xia, Z. (1991). Turbulence characteristics of open-channel flows over rough beds. In *Proceedings of the 24th IAHR Congress* (pp. C33–C40). Madrid: International Association for Hydro-Environment Engineering and Research.

Dwivedi, A. (2014). *Mechanics of Sediment entrainment*. Ph.D. thesis, the University of Auckland, New Zealand.

Dwivedi, A., Melville, B., Raudkivi, A. J., Shamseldin, A. Y., & Chiew, Y. M. (2012). Role of turbulence and particle exposure on entrainment of large spherical particles in flows with low relative submergence. *Journal of Hydraulic Engineering*, *138*(12), 1022–1030. https://doi.org/10.1061/(ASCE)HY.1943-7900.0000632

Dwivedi, A., Melville, B., & Shamseldin, A. Y. (2010). Hydrodynamic forces generated on a spherical sediment particle during entrainment. *Journal of Hydraulic Engineering*, *136*(10), 756–769. https://doi.org/10.1061/(ASCE)HY.1943-7900.0000247

Dwivedi, A., Melville, B. W., Shamseldin, A. Y., & Guha, T. K. (2010). Drag force on a sediment particle from point velocity measurements: A spectral approach. *Water Resources Research*, *46*(10), 1–13. https://doi.org/10.1029/2009WR008643

Fenton, J. D., & Abbott, J. E. (1977). Initial Movement of Grains on a Stream Bed: the Effect of Relative Protrusion. In *Proceedings of the Royal Society of London* (Vol. 352, pp. 523–537).

669 Fischer, P. F., Leaf, G. K., & Restrepo, J. M. (2002). Forces on particles in oscillatory boundary layers.
670 *Journal of Fluid Mechanics*, *468*, 327–347. https://doi.org/10.1017/S0022112002001234

671 Frank, D., Foster, D., Chou, P., Kao, Y.-M., Sou, I. M., & Joseph Calantoni. (2014). Development and
672 evaluation of an autonomous sensor for the observation of sediment motion. *Journal of*
673 *Atmospheric and Oceanic Technology*, *31*(4), 1012–1019. https://doi.org/10.1175/JTECH-D-13-
674 00180.1

675 Frank, D., Foster, D., Sou, I. M., Calantoni, J., & Chou, P. (2014). Lagrangian measurements of
676 incipient motion in oscillatory flows. *Journal of Geophysical Research: Oceans*, *119*(1), 6121–
677 6139. https://doi.org/10.1002/2014JC010105.Received

678 Gendaszek, A. S., Magirl, C. S., Czuba, C. R., & Konrad, C. P. (2013). The timing of scour and fill in
679 a gravel-bedded river measured with buried accelerometers. *Journal of Hydrology*, *495*, 186–196.
680 https://doi.org/10.1016/j.jhydrol.2013.05.012

681 Guan, D., Melville, B. W., & Friedrich, H. (2014). Flow Patterns and Turbulence Structures in a Scour
682 Hole Downstream of a Submerged Weir. *Journal of Hydraulic Engineering*, *140*(1), 68–76.
683 https://doi.org/10.1061/(asce)hy.1943-7900.0000803

684 Kok, M., Hol, J. D., & Schön, T. B. (2017). *Using inertial sensors for position and orientation*
685 *estimation*. *Foundations and Trends in Signal Processing* (Vol. 11).
686 https://doi.org/10.1561/2000000094

687 Kularatna, N., Wijeratne, C., & Melville, B. (2005). Mixed signal approach for rapid prototyping of a
688 compact smart pebble for sediment transport monitoring in river beds. *Proceedings of IEEE*
689 *Sensors, 2005.*, 1128–1132. https://doi.org/10.1109/ICSENS.2005.1597903

690 Lamb, M. P., Brun, F., & Fuller, B. M. (2017). Direct measurements of lift and drag on shallowly
691 submerged cobbles in steep streams: Implications for flow resistance and sediment transport.
692 *Water Resources Research*, *53*(9), 7607–7629. https://doi.org/10.1002/2017WR020883

693 Lamb, M. P., Dietrich, W. E., & Venditti, J. G. (2008). Is the critical shields stress for incipient sediment
694 motion dependent on channel-bed slope? *Journal of Geophysical Research: Earth Surface*, *113*(2),
695 1–20. https://doi.org/10.1029/2007JF000831

696 Lu, W., Melville, B. W., Dawei, G., & Whittaker, C. N. (2018). Local Scour at Downstream Sloped
697 Submerged Weirs. *Journal of Hydraulic Engineering*, *144*(8), 04018044.
698 https://doi.org/10.1061/(asce)hy.1943-7900.0001492

699 Maniatis, G., Hoey, T. B., Hassan, M. A., Sventek, J., Hodge, R., Drysdale, T., & Valyrakis, M. (2017).
700 Calculating the explicit probability of entrainment based on inertial acceleration measurements.
701 *Journal of Hydraulic Engineering*, *143*(4), 1–12. https://doi.org/10.1061/(ASCE)HY.1943-

7900.0001262

Maniatis, G., Hoey, T., Hodge, R., Rickenmann, D., & Badoux, A. (2020). Inertial drag and lift forces for coarse grains on rough alluvial beds. *Earth Surface Dynamics Discussions*, (April), 1–42. https://doi.org/10.5194/esurf-2020-20

Masteller, C. C., & Finnegan, N. J. (2017). Interplay between grain protrusion and sediment entrainment in an experimental flume. *Journal of Geophysical Research: Earth Surface*, *122*(1), 274–289. https://doi.org/10.1002/2016JF003943

McKie, C. W., Juez, C., Plumb, B. D., Annable, W. K., & Franca, M. J. (2021). How Large Immobile Sediments in Gravel Bed Rivers Impact Sediment Transport and Bed Morphology. *Journal of Hydraulic Engineering*, *147*(2), 04020096. https://doi.org/10.1061/(asce)hy.1943-7900.0001842

Nezu, I., & Nakagawa, H. (1993). *Turbulence in open-channel flows*. CRC Press/Balkema, Rotterdam.

Nikora, V. I., Goring, D., McEwan, I., & Griffith, G. (2001). SPATIALLY AVERAGED OPEN-CHANNEL FLOW OVER ROUGH BED. *Journal of Hydraulic Engineering*, *127*(February), 123–133.

Olinde, L., & P.L.Johnson, J. (2015). Using RFID and accelerometer-embedded tracers to measure probabilities of bed load transport, step lengths, and rest times in a mountain stream. *Water Resources Research*, 7572–7589. https://doi.org/10.1002/2015WR017200.A

Paphitis, D. (2001). Sediment movement under unidirectional flows: An assessment of empirical threshold curves. *Coastal Engineering*, *43*(3–4), 227–245. https://doi.org/10.1016/S0378-3839(01)00015-1

Radchenko, A. (2017). Smart rocks for bridge scour montoring-design and localization using electromagnetic techniques and embedded orientation sensors. *Thesis*.

Rahmani, V., Kastens, J. H., de Noyelles, F., Jakubauskas, M. E., Martinko, E. A., Huggins, D. H., … Blackwood, A. J. (2018). Examining storage capacity loss and sedimentation rate of large reservoirs in the Central U.S. great plains. *Water*, *10*(2), 1–17. https://doi.org/10.3390/w10020190

Raus, D., Moulin, F. Y., & Eiff, O. (2019). The Impact of Coarse-Grain Protrusion on Near-Bed Hydrodynamics. *Journal of Geophysical Research: Earth Surface*, *124*(7), 1854–1877. https://doi.org/10.1029/2018JF004751

Recking, A., Piton, G., Vazquez-Tarrio, D., & Parker, G. (2016). Quantifying the Morphological Print of Bedload Transport. *Earth Surface Processes and Landforms*, *41*(6), 809–822. https://doi.org/10.1002/esp.3869

Riebe, C. S., Sklar, L. S., Overstreet, B. T., & Wooster, J. K. (2014). Optimal reproduction in salmon spawning substrates linked to grain size and fish length. *Water Resources Research*, *50*, 898–918.

https://doi.org/10.1002/2013WR014231

Schmeeckle, M. W., Nelson, J. M., & Shreve, R. L. (2007). Forces on stationary particles in near-bed turbulent flows. *Journal of Geophysical Research: Earth Surface*, *112*(2), 1–21. https://doi.org/10.1029/2006JF000536

Shafiei, S., Melville, B. W., Shamseldin, A. Y., Beskhyroun, S., & Adams, K. N. (2016). Measurements of tsunami-borne debris impact on structures using an embedded accelerometer. *Journal of Hydraulic Research*, *54*(4), 435–449. https://doi.org/10.1080/00221686.2016.1170071

Shields, A. (1936). *Awendung der Aehnlichkeitsmechanik und der Turbu-lenzforschung auf die Geschiebebewegung*. PhD Thesis Technical University Berlin.

Spreitzer, G., Tunnicliffe, J. F., & Friedrich, H. (2019). Using Smart Sensors for Measuring Impact Forces of Large Wood (Lw). In *38th IAHR World Congress - "Water: Connecting the World"* (Vol. 38, pp. 3586–3595). Panama. https://doi.org/10.3850/38wc092019-1551

Turowski, J. M., Yager, E. M., Badoux, A., Rickenmann, D., & Molnar, P. (2009). The impact of exceptional events on erosion, bedload transport and channel stability in a step-pool channel. *Earth Surface Processes and Landforms*, *34*, 1661–1673. https://doi.org/10.1002/esp.1855

Wiberg, P. L., & Smith, J. D. (1987). calculations of the critical shear stress for motion of uniform and heterogeneous sediments. *Water Resources Research*, *23*(8), 1471–1480.

Wilcock, P. R., Asce, M., & Crowe, J. C. (2003). Surface-based Transport Model for Mixed-Size Sediment, *129*(February), 120–128.

Wu, F. C., & Chou, Y. J. (2003). Rolling and lifting probabilities for sediment entrainment. *Journal of Hydraulic Engineering*, *129*(2), 110–119. https://doi.org/10.1061/(ASCE)0733-9429(2003)129:2(110)

Yang, Y., Melville, B. W., Sheppard, D. M., & Shamseldin, A. Y. (2019). Live-Bed Scour at Wide and Long-Skewed Bridge Piers in Comparatively Shallow Water. *Journal of Hydraulic Engineering*, *145*(5), 06019005. https://doi.org/10.1061/(ASCE)HY.1943-7900.0001600

Zanke, U. C. E. (2003). On the influence of turbulence on the initiation of sediemnt motion. *International Journal of Sediment Research*, *18*(1), 17–31.